# Realizing Alternagnetism in Fermi-Hubbard Models with Ultracold Atoms

Purnendu Das[1,2,3] Valentin Leeb[1,2] Johannes Knolle[1,2,4] and Michael Knap[1,2]

[1]*Technical University of Munich, TUM School of Natural Sciences, Physics Department, 85748 Garching, Germany*
[2]*Munich Center for Quantum Science and Technology (MCQST), Schellingstr. 4, 80799 München, Germany*
[3]*Indian Institute of Science, Bangalore 560012, India*
[4]*Blackett Laboratory, Imperial College London, London SW7 2AZ, United Kingdom*

Alternagnetism represents a type of collinear magnetism, that is in some aspects distinct from ferromagnetism and from conventional antiferromagnetism. In contrast to the latter, sublattices of opposite spin are related by spatial rotations and not only by translations and inversions. As a result, alternagnets have spin-split bands leading to unique experimental signatures. Here, we show theoretically how a $d$-wave alternagnetic phase can be realized with ultracold fermionic atoms in optical lattices. We propose an alternagnetic Hubbard model with anisotropic next-nearest neighbor hopping and obtain the Hartree-Fock phase diagram. The alternagnetic phase separates in a metallic and an insulating phase and is robust over a large parameter regime. We show that one of the defining characteristics of alternagnetism, the anisotropic spin transport, can be probed with trap-expansion experiments.

*Introduction.*—Collinear quantum magnets are usually assumed to have either ferromagnetic or antiferromagnetic order [1,2]. Ferromagnets break time-reversal symmetry leading to spin-split bands and a net polarization of the magnetic moment. Conventional antiferromagnets exhibit zero net magnetization and are symmetric under translation and spin inversion, leading to spin-degenerate bands. However, recent studies have suggested refinements of this dichotomy and proposed a new class of collinear magnetism, that possess momentum dependent spin-split bands without net magnetization [3–14], as recently confirmed experimentally in material candidates [15–19]. These collinear states, dubbed alternagnets [9,12,13], are characterized by a rotational symmetry of the opposite spin sublattices. For example, in a $d$-wave alternagnet on the square lattice, sublattices are related by a spin flip followed by a $\pi/2$ real-space rotation about a point on the dual lattice; see Fig. 1(a) for an illustration.

Over the recent years, exciting progress has been made in studying quantum magnetism with quantum simulators of ultracold atoms [20]. For the square lattice Hubbard model antiferromagnetic correlations of an extended range have been observed at the lowest experimentally accessible temperatures [21–24] and the consequences of doping the antiferromagnetic state have been investigated [25–28]. Investigating the phenomena of alternagnetism with ultracold atoms remains an interesting open avenue.

In this work, we show how $d$-wave alternagnetism can be realized and characterized with ultracold atoms in optical lattices. We analyze a square lattice Hubbard model with uniform nearest-neighbor and alternating diagonal hoppings and show how this model can be realized by 45° rotated optical lattices. Performing a Hartree-Fock analysis we find that this model stabilizes an alternagnetic phase in an extended parameter range and analyze the robustness of
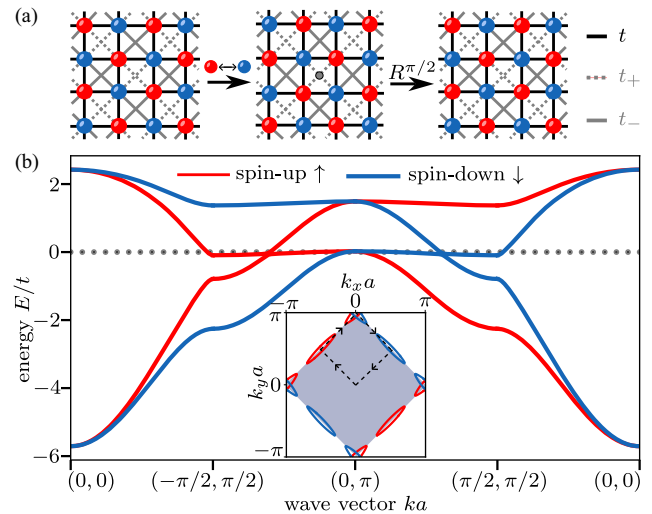


FIG. 1. The alternagnetic Hubbard model. (a) A Néel state on an alternating anisotropic square lattice is a $d$-wave alternagnetic state. It is invariant under a global spin flip (exchanging red and blue dots) followed by a $\pi/2$ real-space rotation around the dual square lattice (gray dot). The nearest-neighbor hopping $t$ and the alternating diagonal hopping $t_\pm$ of the alternagnetic Hubbard model are indicated as well. (b) Spin-resolved band structure of the alternagnetic state at zero temperature for $t'/t = 0.3$, $\delta = 0.9$, $U/t = 3.5$ evaluated along the path indicated in the inset. Inset: Fermi surface and magnetic Brillouin zone (gray shaded area). The band structure obeys the symmetry shown in (a) and is therefore spin-split without net magnetization, which are the key characteristics of an alternagnet.

the state at finite temperatures. We demonstrate that the key experimental characteristic of the altermagnetic state, i.e., the anisotropic spin transport, can be measured by trap-expansion experiments.

*The alternagnetic Hubbard model.*—We consider two species of fermionic atoms labeled by spin $s$ in an optical lattice described by the following altermagnetic Hubbard model

$$\hat{H} = -\sum_{i,j,s} t_{ij}(c_{is}^{\dagger}c_{js} + \text{H.c}) + U\sum_{i} n_{i\uparrow}n_{i\downarrow}, \quad (1)$$

where $U$ is the on-site Hubbard interaction and $t_{ij}$ the hopping matrix element, which is uniform and of strength $t$ for nearest neighbors, sublattice-dependent for diagonal neighbors, and zero otherwise. The diagonal hopping alternates with $t_{\pm} = t'(1 \pm \delta)$ as the following: in the (1,1) direction the hopping element is $t_{-}$ ($t_{+}$) and in the (1,−1) direction it is $t_{+}$ ($t_{-}$) on the $A$ ($B$) sublattice, respectively; see Fig. 1(a).

We consider half-filling $\langle n_i \rangle = \langle n_{i\uparrow} + n_{i\downarrow} \rangle = 1$. However, our results remain qualitatively similar for small doping where the Néel order is stable. We will now show that this particular sublattice dependence of the diagonal hopping leads to altermagnetism and discuss later the optical lattice geometry required to realize this model.

In order to study the magnetic instabilities of our system, we perform a Hartree-Fock analysis that captures the sublattice structure of the $(\pi, \pi)$ magnetic instability. To this end, we introduce the altermagnetic order parameter, $\delta m = (1/4N)\sum_r \langle n_{rA\uparrow} - n_{rA\downarrow} - n_{rB\uparrow} + n_{rB\downarrow}\rangle$, which is proportional to the staggered magnetization. At filling $n$ we write the occupation

$$\langle n_{r\lambda s} \rangle = n/2 + \delta m(-1)^{\lambda+s}, \quad (2)$$

where $r$ denotes the index of a unit cell, $\lambda$ the sublattice, and $s$ the spin. For the alternating sign of the order parameter $(-1)^{\lambda+s}$ we associate $\lambda$ and $s$ with 0 for $A$ and $\uparrow$ and with 1 for $B$ and $\downarrow$, respectively. A nonzero order parameter $\delta m$ indicates a sublattice Néel ordering which in conjunction with the lattice symmetries gives rise to the altermagnetic state. Decoupling the interaction term and expressing it in terms of the mean-field order parameter leads after Fourier transformation to the effective interactions $-U\delta m \sum_k (n_{kA\uparrow} - n_{kB\uparrow} - n_{kA\downarrow} + n_{kB\downarrow})$, where the wave vector $k$ is in the magnetic Brillouin zone. The magnetic Brillouin zone is defined via the real space unit cell spanned by the primitive vectors $a_1 = a(1, 1)$ and $a_2 = a(1, -1)$ with the lattice constant $a$ of the square lattice.

Expressing the mean-field Hamiltonian in the basis of $\Psi_k^{\dagger} = (c_{kA\uparrow}^{\dagger}, c_{kB\uparrow}^{\dagger}, c_{kA\downarrow}^{\dagger}, c_{kB\downarrow}^{\dagger})$, leads to
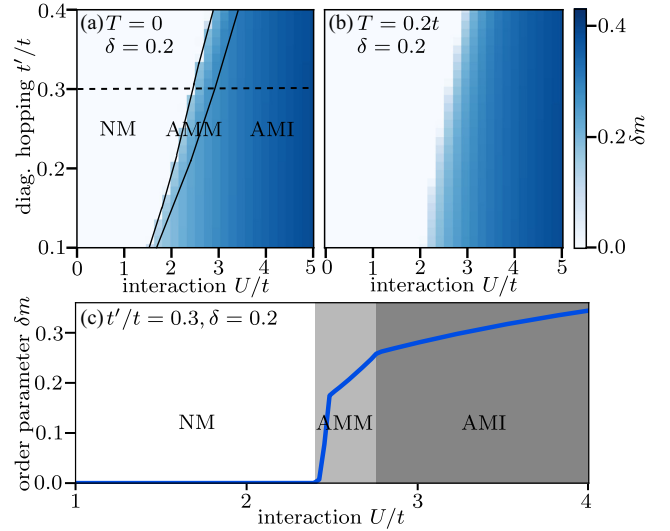


FIG. 2. Robustness of altermagnetism. We compute the altermagnetic order parameter $\delta m$ as a function of interaction strength $U/t$ and diagonal hopping $t'/t$ for staggering $\delta = 0.2$ and temperatures (a) $T = 0$ and (b) $T = 0.2t$. The system is in a normal metallic state when the order parameter vanishes, while a finite order parameter indicates altermagnetic symmetry breaking. (c) Line cut along the dashed line in (a) shows the order parameter at zero temperature for $t'/t = 0.3$ and $\delta = 0.2$. Three phases are distinguished: The normal metal at weak interactions, the altermagnetic metal possessing a Fermi surface at intermediate interactions, and the gapped altermagnetic insulator at strong interactions. Within the AMM the kink in the order parameter at $U/t \approx 2.5$ indicates a Lifshitz transition at which half of the Fermi pockets vanish.

$$\hat{H}^{\text{HF}} = \sum_k \Psi_k^{\dagger} \begin{bmatrix} H_{\uparrow}(k) & 0 \\ 0 & H_{\downarrow}(k) \end{bmatrix} \Psi_k. \quad (3)$$

The Hamiltonian is block diagonal in the spin degree of freedom with $H_s(k) = \begin{bmatrix} h_{AA,s} & h_{AB,s} \\ h_{BA,s} & h_{BB,s} \end{bmatrix}$, where $h_{AA,s} = -2t_{-}\cos(ka_1) - 2t_{+}\cos(ka_2) - (-1)^s U\delta m$, $h_{BB,s} = -2t_{+}\cos(ka_1) - 2t_{-}\cos(ka_2) + (-1)^s U\delta m$, $h_{AB,s} = -2t\cos(k_x a) - 2t\cos(k_y a)$, and $h_{BA,s} = h_{AB,s}^*$. Because of the spin block-diagonal structure of the Hamiltonian (3), bands are fully spin polarized. In addition, each of the spin components exhibit a momentum-inversion symmetry ($k \to -k$) and sublattices are staggered.

We solve the mean-field equations at finite temperatures $T$ by self-consistently determining the order parameter $\delta m = (1/4N)\sum_k \langle n_{kA\uparrow} - n_{kB\uparrow} - n_{kA\downarrow} + n_{kB\downarrow}\rangle_{\text{HF}}$ as well as the chemical potential $\mu$, which is set by fixing the particle number; see Supplemental Material for details [29]. We compute the spin-resolved band structure for $t'/t = 0.3$, $\delta = 0.9$, and $U/t = 3.5$ at half-filling $n = 1$; see Fig. 1(b). Both the band structure and the Fermi surface possess the altermagnetic symmetry of a $\pi/2$ rotation along with a spin flip. Here, the reciprocal lattice vectors of the magnetic

Brillouin zone are $(\pi/2a, \pi/2a)$ and $(\pi/2a, -\pi/2a)$; see shaded area in the inset of Fig. 1(b).

Having established the altermagnetic state, we study its robustness by tuning the system parameters and the temperature. To this end, we compute the order parameter $\delta m$ as a function of $U/t$ and $t'/t$ for $\delta = 0.2$ and $T = 0$ and $0.2t$ in Figs. 2(a) and 2(b). We will show below that the hopping parameters can be controlled by the optical lattice. Moreover, the interaction $U$ is tunable by Feshbach resonances in ultracold atomic systems [30]. The altermagnetic phase is stabilized for increasing diagonal hopping $t'$, staggering $\delta$, and interaction strength $U$. It can be either metallic, characterized by the presence of small Fermi surfaces, or a gapped insulator. A line cut though the phase diagram unveils phase transitions from a normal metal (NM) with vanishing $\delta m$ over an altermagnetic metal (AMM) to an altermagnetic insulator (AMI); see Fig. 2(c). In addition, we find a kink in the order parameter $\delta m$ within the AMM at $U/t \approx 2.5$. This is a Lifshitz transition at which half of the Fermi pockets around $(\pm\pi/2a, \pm\pi/2a)$ disappear. The second kink then indicates the transition from AMM to AMI phase at which the Fermi surfaces disappear. The altermagnetic phase occupies a large portion of the phase diagram, because the underlying mechanism is a consequence of the symmetry of the single-particle band structure. The interactions are only required to establish Néel order, which splits the bands appropriately. The spin splitting is set by the anisotropy of the next-nearest neighbor hopping $t'\delta$. When decreasing $t'\delta$ to zero, the spin-flip and $C_4$-rotation symmetry of the altermagnet regains the spin-flip and translation symmetry, and a conventional antiferromagnet is realized.

*Optical lattice for the altermagnetic band structure.*— The altermagnetic Hubbard model has uniform nearest-neighbor and alternating diagonal hopping elements. Such a single-particle band structure is realized when considering 45°-rotated counterpropagating and phase-locked lasers of wave length $\lambda$ and $2\lambda$ with different strengths, respectively. Specifically, we consider the following lattice potentials

$$V_{\text{latt}} = E_r(V_{\text{sq}} + V_{d,1} + V_{d,2}),$$
$$V_{\text{sq}} = V_0[\sin^2(k_l x) + \sin^2(k_l y)],$$
$$V_{d,1} = V_1\left[\Delta_+\sin^2[k_l(x+y)] + \Delta_-\sin^2\left[\frac{k_l}{2}(x+y)\right]\right],$$
$$V_{d,2} = V_1\left[\Delta_+\sin^2[k_l(x-y)] + \Delta_-\cos^2\left[\frac{k_l}{2}(x-y)\right]\right], \quad (4)$$

where $k_l = 2\pi/\lambda$ is the lattice wave vector, $E_r = (\hbar^2 k_l^2/2m)$ is the recoil energy, $m$ is the mass of the atoms, and $\Delta_\pm = (1 \pm \Delta)$ the potential staggering of strength $\Delta$. The potential consists of deep minima on a square lattice and shallow minima on the dual lattice that are tuned by $V_0$, $V_1$, and $\Delta$; see inset of Fig. 3. For such an optical lattice
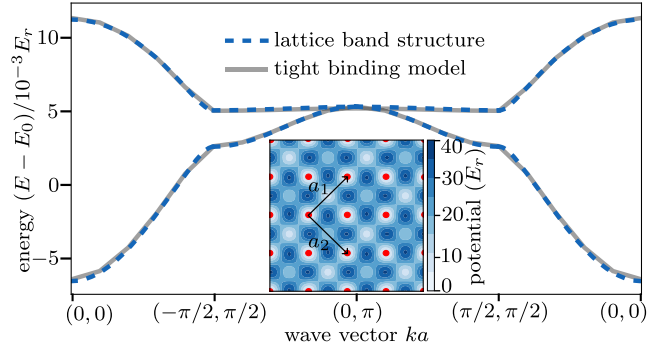


FIG. 3. Effective band structure of the optical lattice. Lowest two bands, solid lines, obtained from solving the Schrödinger equation of a particle in an optical lattice potential with $V_0 = 4E_r$, $V_1/V_0 = 2.2$, and $\Delta = 0.6$; see Eq. (4). Bands obtained from a tight-binding model with uniform nearest-neighbor hopping $t$ and the alternating diagonal hopping amplitudes $t_\pm = t'(1 \pm \delta)$, dashed line, agree well with the full band structure. The effective parameters of the tight-binding model are $t = 2.2 \times 10^{-3}E_r$, $t'/t = 0.16$, $\delta = 0.83$ and the energy offset is $E_0 = 13.81E_r$. Inset: Illustration of the optical lattice potential.

both the nearest neighbor and the diagonal tunneling are sizeable.

The unit cell of the lattice is $\sqrt{2}a \times \sqrt{2}a$, where $a$ is the lattice constant of the square lattice, with primitive lattice vectors $a_1$ and $a_2$; see inset of Fig. 3. We numerically solve the Schrödinger equation of a single particle in this optical lattice potential by standard techniques (see, e.g., Ref. [31]) and show the lowest two bands in Fig. 3. We then fit the lowest bands to the tight-binding Hamiltonian of the altermagnetic Hubbard model and obtain the uniform nearest-neighbor hopping $t$ and the staggered diagonal hoppings $t_\pm = t'(1 \pm \delta)$. The diagonal hopping elements are sizable for this lattice because of the potential minima at the dual lattice sites. The tight-binding band structure reproduces well the lowest two bands; Fig. 3. The tight-binding parameters are tunable by $V_0$, $V_1$, and $\Delta$ which characterize the optical lattice; see Supplemental Material [29]. Here, we have considered deep optical lattices, leading to comparatively low absolute scales of the hopping. Shallower lattices provide larger absolute hopping scales, while at the same time giving rise to longer-ranged hoppings. As a consequence, more complex tight-binding models are needed for quantitative agreement. However, we find that the band structure of shallower lattice potentials still posses the same symmetries and the same anisotropic behavior as the deep lattice; see Supplemental Material [29]. Larger effective energy scales will be advantageous in experiments to access the required temperatures and obtain homogeneous parameters throughout the system.

*Experimental signatures.*—The altermagnetic state manifests itself in a vanishing net magnetization but has a

pronounced spin-polarized Fermi surface, which can be probed by spin-resolved transport [6,32]. One way to probe such anomalous transport with ultracold atoms is to release the trapping potential and to subsequently measure the spin-resolved densities while the atomic cloud expands; see, e.g., Refs. [33–37]. To characterize such an expansion experiment, we first determine the conductivity tensor and then use Einstein's relation for the diffusion constant to obtain an effective hydrodynamic description of the expansion dynamics.

The conductivity tensor for both spin-up and spin-down atoms are $2 \times 2$ matrices with elements $\sigma_{\alpha\beta}^s$, where $\alpha, \beta \in \{\tilde{x}, \tilde{y}\}$ indicate the spatial direction along the primitive lattice vectors $\{a_1, a_2\}$ of the two-site unit cell and $s \in \{\uparrow, \downarrow\}$ is the spin state. Since the bands are fully spin polarized, the conductivity is diagonal in spin basis, see Eq. (3). The transverse Hall contribution to the conductivity vanishes, $\sigma_{\alpha\beta}^s = 0$ for $\alpha \neq \beta$, due to the momentum-inversion symmetry of Eq. (3). From the spin-flip and $\pi/2$ rotation symmetry in real space, we further deduce that the conductivity tensor of spin-up and spin-down are related by $\sigma_{\alpha\alpha}^\uparrow = \sigma_{\bar{\alpha},\bar{\alpha}}^\downarrow$, where $\bar{\alpha}$ is the direction orthogonal to $\alpha$. We use the Kubo formula to evaluate the diagonal dc conductivity tensor [38–40], see also Supplemental Material [29]

$$\sigma_{\alpha\alpha}^s = -\frac{\hbar}{\pi V} \int_{-\infty}^{\infty} d\epsilon \frac{df}{d\epsilon} \sum_{m,n,k} |\langle \psi_m(\boldsymbol{k})|v_\alpha^s|\psi_n(\boldsymbol{k})\rangle|^2$$

$$\times \frac{\Gamma}{(\epsilon - \epsilon_n)^2 + \Gamma^2} \frac{\Gamma}{(\epsilon - \epsilon_m)^2 + \Gamma^2}, \quad (5)$$

where $v_\alpha^s = (1/\hbar)\nabla_{k_\alpha} H_s(\boldsymbol{k})$ is the spin dependent velocity, $f$ is the Fermi-Dirac distribution function, $\epsilon_n$ and $|\psi_n(\boldsymbol{k})\rangle$ are the eigenenergies and eigenstates of Eq. (3), respectively, $\Gamma$ is an positive infinitesimal that we use for the numerical evaluation of the integral.

In order to compute the relaxation dynamics, we relate the conductivity matrix with the diffusion matrix by the Einstein relation [38],

$$\sigma_{\alpha\beta}^s = \frac{n^s D_{\alpha\beta}^s}{T}, \quad (6)$$

where $n^s$ is the particle density of spin $s$ atoms and $T$ is the temperature. Our model conserves the densities of both spin species separately, leading to the continuity equation $(\partial n^s/\partial \tau) + \nabla \boldsymbol{J}^s = 0$, where $\tau$ denotes real time. Taking the hydrodynamic assumption, we perform a gradient expansion of the currents. Because of the symmetries of the conductivity tensor, only diagonal contributions arise and the currents are related to the density gradients as $J_\alpha^s = -D_{\alpha\alpha}\partial_\alpha n^s$, where $\alpha \in \{\tilde{x}, \tilde{y}\}$. We thus obtain the diffusion equation
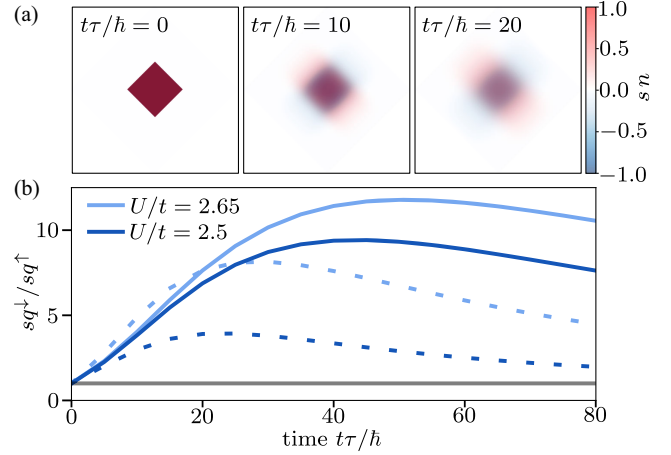


FIG. 4. Anisotropic spin diffusion. (a) Trap-release dynamics of an altermagnetic state at finite temperature $T = 0.2t$, trapped in a box potential in an optical lattice characterized by $V_0 = 4E_r$, $V_1/V_0 = 2.2$, $\Delta = 0.6$. The spin-resolved density propagates anisotropically in real space along the $a_1$ and $a_2$ directions. (b) We characterize the anisotropic expansion by the ratio of the geometric squeezing parameter $sq^s(\tau)$ of spin-down and spin-up atoms for two different values of the interaction $U$ and two different temperatures $T = 0.15t$ (solid lines) and $T = 0.2t$ (dashed lines). The gray line represents the isotropic expansion of a normal metallic state for which $sq^s(\tau)$ is always one.

$$\frac{\partial n^s}{\partial \tau} = (D_{\tilde{x}\tilde{x}}^s \partial_{\tilde{x}}^2 + D_{\tilde{y}\tilde{y}}^s \partial_{\tilde{y}}^2) n^s. \quad (7)$$

As the diffusion constants are anisotropic in space, the transport of spin will be anisotropic as well. This is a key signature of the altermagnetic state. In order to demonstrate this behavior, we initialize our system at temperature $T = 0.2t$ in the optical potential characterized by $V_0 = 4E_r$, $V_1/V_0 = 2.2E_r$, $\Delta = 0.6$, and $\lambda = 1064$ nm at half-filling inside the square-shaped region; for the temperature dependence of the conductivity see Supplemental Material [29]. Subsequently, we let the particles expand by removing the trapping potential at time $\tau = 0$ and compute the time evolution of the spin-resolved densities by numerically solving the diffusion equation (7); Fig. 4(a).

We observe that the spin-up and spin-down atoms predominantly relax in different directions, related by a $\pi/2$ real-space rotation. The spin-up atoms have a larger contribution to $\sigma_{\tilde{y}\tilde{y}}^\uparrow$ than $\sigma_{\tilde{x}\tilde{x}}^\uparrow$ as can be also seen from the Fermi surface in the inset of Fig. 1(b). Thus diffusion is stronger in the $a_2$ direction than in $a_1$ direction and vice versa for spin-down atoms. To quantify the anisotropy, we define a geometric squeezing parameter

$$sq^s(\tau) = \frac{\int d^2\tilde{r}\tilde{x}^2 n^s(\tilde{\boldsymbol{r}}, \tau)}{\int d^2\tilde{r}\tilde{y}^2 n^s(\tilde{\boldsymbol{r}}, \tau)}, \quad (8)$$

which measures the relative spread in $\tilde{x}$ direction compared to the $\tilde{y}$ direction. The relative squeezing of spin-down and

spin-up $sq^\downarrow(\tau)/sq^\uparrow(\tau)$ initially increases strongly and then approaches one asymptotically because the steady state is uniform in space; Fig. 4(b).

When increasing the interaction strength $U$ the alter-magnetic order parameter increases and by consequence also the spin-splitting energy, which leads to a larger squeezing parameter. For higher temperatures the anisotropy in the conductivity tensor is reduced as the spin splitting decreases. However, the initial growth of $sq^\downarrow(\tau)/sq^\uparrow(\tau)$ can be larger as overall the diffusion constant increases with temperature according to the Einstein relation. Although we assume the experiment to be performed in a box potential, one could also release a harmonic confinement potential [37]. The central idea is to observe the anisotropic spin diffusion which is a character-istic of the alternmagnetic phase.

*Conclusions and outlook.*—Altermagnetism represents a type of collinear magnetism, that is characterized by rotational symmetries between opposite spin sublattices. We have shown how such an altermagnetic state can be realized with fermionic ultracold atoms. As the underlying mechanism derives from the single-particle band structure, the state is robust and arises over a large parameter range. We discuss that the unconventional symmetry of the state can be detected experimentally in trap expansion experi-ments which exhibit anisotropic expansion for the different spin species.

Signatures of the altermagnetic state can also be obtained with quantum gas microscopes [41,42]. The order param-eter, i.e., the staggered magnetization, can be measured directly as a real space Néel pattern [24]. In addition, anisotropic local current distributions need to be estab-lished for altermagnetism. The rung current can be mea-sured in quantum gas microscopes, by freezing the states into double wells and subsequently performing a $\pi/4$ tunneling event in each double well. This maps the rung current to the occupation basis [43] from which the altermagnetic symmetries can be deduced.

Our work demonstrates the potential for ultracold atoms to provide a controllable platform for realizing and probing this new form of magnetism and for understanding the structure of fluctuations around the ordered states. For future work it would be interesting to characterize the anisotropic spin susceptibilities of the altermagnetic state, which can be measured, for example, by Ramsey interferometry [44] or modulation spectroscopy [45]. Furthermore, the real-time dynamics of spin-wave excitations in the altermagnetic insulating state could unveil the unconventional symmetry of the state as well. An exciting direction is to explore the interplay of doped altermagnets and competing supercon-ducting instabilities, which may offer a route to realize finite-momentum pairing or topological superconductivity.

Numerical data and simulation codes are available on Zenodo [46].

[1] N. W. Ashcroft and N. D. Mermin, *Solid State Physics* (Cengage Learning, Fort Worth, 2022).

[2] A. Auerbach, *Interacting Electrons and Quantum Magnet-ism* (Springer Science & Business Media, New York, 1998).

[3] C. Wu, K. Sun, E. Fradkin, and S.-C. Zhang, Fermi liquid instabilities in the spin channel, Phys. Rev. B **75**, 115103 (2007).

[4] K.-H. Ahn, A. Hariki, K.-W. Lee, and J. Kuneš, Antiferro-magnetism in $RuO_2$ as $d$-wave Pomeranchuk instability, Phys. Rev. B **99**, 184432 (2019).

[5] S. Hayami, Y. Yanagi, and H. Kusunose, Momentum-dependent spin splitting by collinear antiferromagnetic ordering, J. Phys. Soc. Jpn. **88**, 123702 (2019).

[6] L. Šmejkal, R. González-Hernández, T. Jungwirth, and J. Sinova, Crystal time-reversal symmetry breaking and spon-taneous Hall effect in collinear antiferromagnets, Sci. Adv. **6**, eaaz8809 (2020).

[7] S. Hayami, Y. Yanagi, and H. Kusunose, Bottom-up design of spin-split and reshaped electronic band structures in antiferromagnets without spin-orbit coupling: Procedure on the basis of augmented multipoles, Phys. Rev. B **102**, 144441 (2020).

[8] I. I. Mazin, K. Koepernik, M. D. Johannes, R. González-Hernández, and L. Šmejkal, Prediction of unconventional magnetism in doped fesb2, Proc. Natl. Acad. Sci. U.S.A. **118**, e2108924118 (2021).

[9] L. Šmejkal, J. Sinova, and T. Jungwirth, Beyond conven-tional ferromagnetism and antiferromagnetism: A phase with nonrelativistic spin and crystal rotation symmetry, Phys. Rev. X **12**, 031042 (2022).

[10] D. Shao, S. Zhang, and M. e. a. Li, Spin-neutral currents for spintronics, Nat. Commun. **12**, 7061 (2021).

[11] L. Šmejkal, A. B. Hellenes, R. González-Hernández, J. Sinova, and T. Jungwirth, Giant and tunneling magneto-resistance in unconventional collinear antiferromagnets with nonrelativistic spin-momentum coupling, Phys. Rev. X **12**, 011028 (2022).

[12] L. Šmejkal, J. Sinova, and T. Jungwirth, Emerging research landscape of altermagnetism, Phys. Rev. X **12**, 040501 (2022).

[13] I. Mazin (The PRX Editors), Editorial: Altermagnetism—a new punch line of fundamental magnetism, Phys. Rev. X **12,** 040002 (2022).

[14] T. A. Maier and S. Okamoto, Weak-coupling theory of neutron scattering as a probe of altermagnetism, Phys. Rev. B **108,** L100402 (2023).

[15] J. Krempaský et al., Altermagnetic lifting of Kramers spin degeneracy, arXiv:2308.10681.

[16] S. Lee, S. Lee, S. Jung, J. Jung, D. Kim, Y. Lee, B. Seok, J. Kim, B. G. Park, L. Šmejkal, C.-J. Kang, and C. Kim, Broken Kramers' degeneracy in altermagnetic MnTe, Phys. Rev. Lett. **132,** 036702 (2024).

[17] S. Reimers, L. Odenbreit, L. Smejkal, V. N. Strocov, P. Constantinou, A. B. Hellenes, R. J. Ubiergo, W. H. Campos, V. K. Bharadwaj, A. Chakraborty, T. Denneulin, W. Shi, R. E. Dunin-Borkowski, S. Das, M. Kläui, J. Sinova, and M. Jourdan, Direct observation of altermagnetic band splitting in CrSb thin films, Nat. Commun. **15,** 2116 (2024).

[18] Z. Feng, X. Zhou, L. Šmejkal, L. Wu, Z. Zhu, H. Guo, R. González-Hernández, X. Wang, H. Yan, P. Qin, X. Zhang, H. Wu, H. Chen, Z. Meng, L. Liu, Z. Xia, J. Sinova, T. Jungwirth, and Z. Liu, An anomalous Hall effect in altermagnetic ruthenium dioxide, National electronics review **5,** 735 (2022).

[19] X. Zhou, W. Feng, R.-W. Zhang, L. Šmejkal, J. Sinova, Y. Mokrousov, and Y. Yao, Crystal thermal transport in altermagnetic $RuO_2$, Phys. Rev. Lett. **132,** 056701 (2024).

[20] I. Bloch, J. Dalibard, and W. Zwerger, Many-body physics with ultracold gases, Rev. Mod. Phys. **80,** 885 (2008).

[21] R. Jördens, N. Strohmaier, K. Günter, H. Moritz, and T. Esslinger, A Mott insulator of fermionic atoms in an optical lattice, Nature (London) **455,** 204 (2008).

[22] U. Schneider, L. Hackermüller, S. Will, T. Best, I. Bloch, T. A. Costi, R. W. Helmes, D. Rasch, and A. Rosch, Metallic and insulating phases of repulsively interacting fermions in a 3d optical lattice, Science **322,** 1520 (2008).

[23] R. A. Hart, P. M. Duarte, T.-L. Yang, X. Liu, T. Paiva, E. Khatami, R. T. Scalettar, N. Trivedi, D. A. Huse, and R. G. Hulet, Observation of antiferromagnetic correlations in the Hubbard model with ultracold atoms, Nature (London) **519,** 211 (2015).

[24] A. Mazurenko, C. S. Chiu, G. Ji, M. F. Parsons, M. Kanász-Nagy, R. Schmidt, F. Grusdt, E. Demler, D. Greif, and M. Greiner, A cold-atom Fermi–Hubbard antiferromagnet, Nature (London) **545,** 462 (2017).

[25] C. S. Chiu, G. Ji, A. Bohrdt, M. Xu, M. Knap, E. Demler, F. Grusdt, M. Greiner, and D. Greif, String patterns in the doped Hubbard model, Science **365,** 251 (2019).

[26] A. Bohrdt, C. S. Chiu, G. Ji, M. Xu, D. Greif, M. Greiner, E. Demler, F. Grusdt, and M. Knap, Classifying snapshots of the doped Hubbard model with machine learning, Nat. Phys. **15,** 921 (2019).

[27] J. Koepsell, D. Bourgund, P. Sompet, S. Hirthe, A. Bohrdt, Y. Wang, F. Grusdt, E. Demler, G. Salomon, C. Gross, and I. Bloch, Microscopic evolution of doped Mott insulators from polaronic metal to Fermi liquid, Science **374,** 82 (2021).

[28] A. Bohrdt, L. Homeier, C. Reinmoser, E. Demler, and F. Grusdt, Exploration of doped quantum magnets with ultracold atoms, Ann. Phys. (Amsterdam) **435,** 168651 (2021).

[29] See Supplemental Material at http://link.aps.org/supplemental/10.1103/PhysRevLett.132.263402 for the self-consistent Hartree-Fock equations, the tight-binding parameters, the optical lattice potential, the evaluation of the conductivity tensor, and its temperature dependence.

[30] C. Chin, R. Grimm, P. Julienne, and E. Tiesinga, Feshbach resonances in ultracold gases, Rev. Mod. Phys. **82,** 1225 (2010).

[31] U. Bissbort, Dynamical Effects and Disorder in Ultracold Bosonic Matter, doctoralthesis, Universitätsbibliothek Johann Christian Senckenberg, 2013.

[32] R. González-Hernández, L. Šmejkal, K. Výborný, Y. Yahagi, J. Sinova, T. c. v. Jungwirth, and J. Železný, Efficient electrical spin splitter based on nonrelativistic collinear antiferromagnetism, Phys. Rev. Lett. **126,** 127701 (2021).

[33] A. Sommer, M. Ku, G. Roati, and M. W. Zwierlein, Universal spin transport in a strongly interacting Fermi gas, Nature (London) **472,** 201 (2011).

[34] U. Schneider, L. Hackermüller, J. P. Ronzheimer, S. Will, S. Braun, T. Best, I. Bloch, E. Demler, S. Mandt, D. Rasch, and A. Rosch, Fermionic transport and out-of-equilibrium dynamics in a homogeneous Hubbard model with ultracold atoms, Nature (London) **8,** 213 (2012).

[35] P. T. Brown, D. Mitra, E. Guardado-Sanchez, R. Nourafkan, A. Reymbaut, C.-D. Hébert, S. Bergeron, A.-M. S. Tremblay, J. Kokalj, D. A. Huse, P. Schauß, and W. S. Bakr, Bad metallic transport in a cold atom Fermi-Hubbard system, Science **363,** 379 (2019).

[36] M. A. Nichols, L. W. Cheuk, M. Okan, T. R. Hartke, E. Mendez, T. Senthil, E. Khatami, H. Zhang, and M. W. Zwierlein, Spin transport in a Mott insulator of ultracold fermions, Science **363,** 383 (2019).

[37] N. Darkwah Oppong, G. Pasqualetti, O. Bettermann, P. Zechmann, M. Knap, I. Bloch, and S. Fölling, Probing transport and slow relaxation in the mass-imbalanced Fermi-Hubbard model, Phys. Rev. X **12,** 031026 (2022).

[38] R. Kubo, Statistical-mechanical theory of irreversible processes. I. General theory and simple applications to magnetic and conduction problems, J. Phys. Soc. Jpn. **12,** 570 (1957).

[39] A. Crépieux and P. Bruno, Theory of the anomalous Hall effect from the Kubo formula and the Dirac equation, Phys. Rev. B **64,** 014416 (2001).

[40] F. Freimuth, S. Blügel, and Y. Mokrousov, Spin-orbit torques in Co/Pt(111) and Mn/W(001) magnetic bilayers from first principles, Phys. Rev. B **90,** 174423 (2014).

[41] W. S. Bakr, J. I. Gillen, A. Peng, S. Fölling, and M. Greiner, A quantum gas microscope for detecting single atoms in a Hubbard-Regime optical lattice, Nature (London) **462,** 74 (2009).

[42] J. F. Sherson, C. Weitenberg, M. Endres, M. Cheneau, I. Bloch, and S. Kuhr, Single-atom-resolved fluorescence imaging of an atomic Mott insulator, Nature (London) **467,** 68 (2010).

[43] E. Wybo, A. Bastianello, M. Aidelsburger, I. Bloch, and M. Knap, Preparing and analyzing solitons in the Sine-Gordon

model with quantum gas microscopes, PRX Quantum **4,** 030308 (2023).

[44] M. Knap, A. Kantian, T. Giamarchi, I. Bloch, M. D. Lukin, and E. Demler, Probing real-space and time-resolved correlation functions with many-body ramsey interferometry, Phys. Rev. Lett. **111,** 147205 (2013).

[45] A. Bohrdt, D. Greif, E. Demler, M. Knap, and F. Grusdt, Angle-resolved photoemission spectroscopy with quantum gas microscopes, Phys. Rev. B **97,** 125117 (2018).

[46] P. Das, V. Leeb, J. Knolle, and M. Knap, All data and simulation codes are available upon reasonable request at 10.5281/zenodo.10391823 (2024).